Materials Advances

ROYAL SOCIETY OF CHEMISTRY

PAPER

View Article Online
View Journal | View Issue

Cite this: *Mater. Adv.*, 2024, 5, 2872

Enhanced $LiMn_2O_4$ cathode performance in lithium-ion batteries through synergistic cation and anion substitution†

Oyunbayar Nyamaa,[a] Hyo-Min Jeong,[a] Gyeong-Ho Kang,[b] Jung-Soo Kim,[a] Kyeong-Mo Goo,[a] In-Gyu Baek,[a] Jeong-Hyeon Yang,[c] Tae-Hyun Nam[b] and Jung-Pil Noh*[a]

Received 31st December 2023,
Accepted 9th February 2024

DOI: 10.1039/d3ma01187a

rsc.li/materials-advances

The use of lithium-ion batteries (LIBs) continues to grow to overcome environmental challenges, and spinel $LiMn_2O_4$ is employed as a high-performance and safe electrode material in this context. In this study, we introduce a novel multi-substituted spinel by partially replacing manganese (Mn^{4+}) with titanium (Ti^{4+}) and oxygen (O^{2-}) with sulfur (S^{2-}) at the octahedral 16d and 32e sites. We explore the substitution with Ti alone and the intricate synergistic effects resulting from the simultaneous multisubstitution with Ti and S. These synergistic effects are designed to enhance the electrochemomechanical properties and prolong the life cycle of spinel $LiMn_2O_4$. This approach stabilizes the structure by mitigating the Jahn–Teller distortion and maintains capacity integrity throughout the spinel's operational lifespan. We synthesize spinel $LiMn_2O_4$ by using the sol–gel method and investigate the synergistic effects of Ti and S substitution on the structural, morphological, and electrochemical attributes of the $LiMn_2O_4$ cathode. The electrochemical properties show that the new strategy leads to enhanced optimization, structural stability, and cycling performance. The rate capability of the $LiMn_{1.78}Ti_{0.22}O_{3.97}S_{0.03}$ cathode with Ti and S substitution is observed, where the 10th discharge capacity is 114 mA h g^{-1} at 5C and charge/discharge capacity is 123/122 mA h g^{-1} after 500 cycles with a capacity retention of 90.3%, which is significantly higher than the capacity retentions of $LiMn_{1.8}Ti_{0.22}O_4$ (76.6%) and non-substituted $LiMn_2O_4$ (33.9%).

Introduction

Lithium-ion batteries (LIBs) are widely used in electric vehicles and portable devices owing to their diversity, high energy (W h kg^{-1}) and power densities (W kg^{-1}), and long cycle life. The development of LIBs with high specific power densities and long cycle lives involve advancements in various areas, such as electrode materials, cell design, and manufacturing processes. Spinel $LiMn_2O_4$ is a potential candidate for replacing layered Ni or Co oxide materials as cathodes and can achieve a balance between performance, cost-effectiveness, environmental friendliness, and safety.[1] However, the practical applications of $LiMn_2O_4$ cathodes are restricted because of capacity fading during cycling. This capacity fading is attributed to two main factors: Mn dissolution and Jahn–Teller distortion.[2] In certain transition metal (TM) scenarios, the occupancy of electron-filled orbitals can influence the local structure, prompting geometric distortions around the TM ion. An illustrative example of a J–T ion is Mn^{3+}, as depicted in Fig. S1 (ESI†). The J–T distortion manifests due to electronic degeneracy in specific TM ions, notably Mn^{3+}, and is intensified by the presence of trace amounts of hydrofluoric acid (HF) generated within the electrolyte. Specifically, when the ion adopts a high-spin configuration within an octahedral ligand field (LF), it possesses a lone electron in the upper e_g state. Introducing a tetragonal distortion becomes energetically favorable, achieved by lengthening the bond along the *z*-axis and lowering the energy of the system. This lowering in total energy results from the downward repositioning of one of the e_g orbitals, with the t_{2g} state remaining unsplit due to the preservation of its center of gravity. In this case, the J–T distortion situates an electron into the d_{z^2} orbital, which exhibits weak interaction with axial oxygens, inducing a heightened negative charge on these oxygens and an increase in acidity. The resulting acidic conditions, stemming from the hydrolysis of $LiPF_6$ salt in the electrolyte,

[a] Department of Energy and Mechanical Engineering and Institute of Marine Industry, Gyeongsang National University, 2 Tongyeonghaean-to, Tongyeong 53064, Korea. E-mail: nohjp@gnu.ac.kr
[b] Department of Materials Engineering and Convergence Technology, Gyeongsang National University, Jinju-daero 501, Jinju 52828, Korea
[c] Department of Mechanical System Engineering, Gyeongsang National University, 2 Tongyeonghaean-to, Tongyeong 53064, Korea

† Electronic supplementary information (ESI) available. See DOI: https://doi.org/10.1039/d3ma01187a

facilitate the dissolution of metal ions from transition metal oxides (TMOs) harboring J–T ions. These dissolved metal ions, in a cyclical fashion, contribute to the deterioration of the electrolyte and the overall components of the battery.[3] Various strategies have been explored to mitigate these issues and improve the performance of $LiMn_2O_4$ cathodes.[4–12] These include surface coating techniques for reducing Mn dissolution, doping or modifying the cathode structure to minimize Jahn–Teller distortion, and optimizing the electrolyte composition to mitigate side reactions.[13] One successful strategy is substituting Mn with Ti^{4+} ions in $LiMn_2O_4$; this contributes to reduced capacity fading and improved cycling stability in LIBs.[7,14,15] The presence of Ti^{4+} stabilizes the crystal structure and reduces the reactivity of Mn with the electrolyte, leading to decreased Mn dissolution and improved cycling stability.[15,16] Pure $LiMn_2O_4$ is susceptible to structural transformations during charge–discharge cycles, leading to capacity fading. When Ti ions are incorporated into the $LiMn_2O_4$ structure, the Ti–O bonds (Ti–O (662 kJ mol^{-1}) > Mn–O (402 kJ mol^{-1})) contribute to stronger interatomic interactions within the crystal lattice.[17] This increased bonding strength helps to stabilize the crystal structure and reduce structural transformations during charge–discharge cycles. The enhanced structural stability contributes to improved cycling performance and reduced capacity fading in Ti-substituted $LiMn_2O_4$ ($[Mn_{2-x}Ti_x]O_4$) cathodes.[15] An essential attribute of a cathode material is its capability to store a substantial amount of reversible energy within the electrochemical potential gap. This capability is determined based on a material's maximum energy storage limit, which represents the maximum reusable energy during battery discharge, as defined in the following equation:[18]

$$Wh_{th} = \frac{ne^- F}{3.6 \times M}, \quad (1)$$

where ne^- is the number of electrons released per unit mole, F is the Faraday constant, and M is the cathode molecular mass. A conversion factor of 3.6 is applied to transform the energy capacity from Coulomb per second to mA h g^{-1}. The number of electrons in the cathode material is influenced by the change in the ionic charge of the transition metal, which determines the number of Li ions that can be accommodated per unit of chemical formula. For example, in the non-substituted $LiMn_2O_4$ (LMO) spinel, Mn^{4+} is converted to Mn^{3+} during discharge, allowing only one Li ion to be accommodated. According to eqn (1), structures with lower molar masses and more active electrons have a higher energy storage capacity. Thus, the incorporation of Ti, which has a low molar mass, is favorable. Furthermore, the equation reveals that the extensive substitution of electrochemically active elements diminish the energy storage capacity by lowering the number of active electrons. Consequently, additional research is imperative to address the capacity challenges arising from the electrochemical inactivity of these dopant ions. Anionic substitution (F, S) in the oxygen sublattice is a potential method for overcoming this problem without losing the capacity to increase the structural strength and cycling stability of $LiMn_2O_4$.[6,19,20] Among many anion species, S substitution is efficient in improving the rate capability and cyclic performance.[6] In the investigation of the $LiNi_xMn_{2-x}O_{4-\delta}S_\delta$ system ($0 \le x \le 0.5$ and $0 \le \delta \le 0.1$), Raja *et al.*[21] noted a reduction in lattice constant as nickel content increased. This observation is tentatively attributed to an elevated concentration of Mn^{4+}. The authors propose that this phenomenon is likely influenced by the catalytic activity of sulfur within the octahedra of the spinel matrix. Another factor in reducing Jahn–Teller distortion is that the atomic radius of sulfur is larger than that of oxygen and leads to lattice expansion and structural transformations during charge–discharge cycles.[13,22–24] This expansion can contribute to improved cycling stability and capacity retention. Furthermore, S substitution can suppress the dissolution of Mn ions from the $LiMn_2O_4$ cathode into the electrolyte. S substitution can efficiently improve the electrochemical performance (rate capability and cyclic performance) because easy Li^+ intercalation and extraction are expected owing to lattice expansion and the lower bond dissociation energy of Li–S (312.5 kJ mol^{-1}) than of Li–O (340.5 kJ mol^{-1}).[20] S substitution has been found to be very effective in suppressing the formation of the tetragonal phase of $LiMn_2O_4$ at close to room temperature.[23,25] In addition, the introduction of sulfur ions modifies the local environment and creates additional lithium diffusion pathways within the material. These advantages make S multisubstitution in $LiMn_2O_4$ a promising strategy for enhancing performance. Multisubstitution with both anions and cations can create synergistic effects that cannot be achieved with a single substituent ion.[26–28] The combination of different substituent ions in the crystal lattice can target different aspects of the cathode material, such as the lattice expansion, strength, and stability, electronic conductivity, lithium diffusion, and surface area. Cooperative interactions between anions and cations can provide unique benefits beyond the effects of a single substituent. Here, we introduce a pioneering approach by developing a novel class of multi-substituted spinel, denoted as ($Li(Mn^{3+}Mn^{4+}_{2-x}Ti_x)O_{4-y}S_y$). We focus on not only Ti but also the synergistic effects arising from co-substitution with Ti and S. The collaboration of these elements leads to significant enhancements in both electrochemical performance and structural stability but has not been explored yet. The novel class of multi-substituted spinel is successfully synthesized using the sol–gel method. The synergistic effects of Ti and S are investigated by performing field-emission scanning electron microscopy (FE-SEM), X-ray diffraction (XRD), high-resolution transmission electron microscopy (HR-TEM), X-ray photoelectron spectroscopy (XPS) and electrochemical characterizations.

Experimental details

Materials

Reagents with a purity of approximately 99.99% were used without further purification. Lithium acetate dihydrate ($CH_3COOLi{\cdot}2H_2O$), manganese acetate tetrahydrate ($(CH_3COO)_2Mn{\cdot}4H_2O$), titanium(IV) *n*-butoxide ($C_{18}H_{36}O_4Ti$), and ethylene glycol ($HOCH_2CH_2OH$) were purchased from Seohaean-ro Siheung-si, Gyeonggi-

do, Republic of Korea. Ammonium sulfide solution ($(NH_4)_2S$) and citric acid $C_3H_4OH(COOH)_3$ were purchased from Nihonbashi-honcho, Chuoku, Tokyo, Japan. Li foil and coin cells (CR 2032) were purchased from Wellcos Corporation, Ltd. (South Korea) for battery assembly. An electrolyte solution of 1 M $LiPF_6$ in ethylene carbonate (EC) : diethyl carbonate (DEC) (1 : 1 vol%) was purchased from Soulbrain Co., Ltd. (South Korea).

Preparation of $LiMn_2O_4$ particles

Spinel $LiMn_2O_4$ nanoparticles were synthesized by using the sol–gel method. $CH_3COOLi{\cdot}2H_2O$ and $(CH_3COO)_2Mn{\cdot}4H_2O$ were used as precursor sources. Citric acid $C_3H_4OH(COOH)_3$ and ethylene glycol ($HOCH_2CH_2OH$) were used as the chelating agent and polymerization monomer, respectively. The stoichiometric ratio of 1 mol (M) of $CH_3COOLi{\cdot}2H_2O$ and 2 mol (M) of $(CH_3COO)_2Mn{\cdot}4H_2O$ was dissolved in deionized water (just before saturation). A separately prepared 30% citric acid solution in water was then added dropwise to the aforementioned prepared solution. The molar ratio of citric acid to total cations was 1 : 1. Subsequently, 6 mol of ethylene glycol was combined with a solution of the obtained metal citric complex. This esterification reaction led to the formation of a cross-linked polymer gel. Utilizing a polymer-like structure in the sol–gel form can achieve a uniform distribution of cations in $LiMn_2O_4$.[29,30] Then, the solution was (referred to as LMO solution) heated to react at 120 °C under stirring, and the esterification and polymerization processes were continued until a dark brown viscous gel was obtained. The resultant gel was dried at 120 °C in an oven for 15 h and then ground. The calcination process was then performed in an oxygen atmosphere at a temperature of 400 °C for 5 h and at 700 °C for 15 h. After being naturally cooled to 25 °C, the final product was ground and the nanoparticles were designated as LMO.

Preparation of Ti-substituted $LiMn_2O_4$ and Ti–S-substituted $LiMn_2O_4$ particles

Ti-substituted $LiMn_{1.78}Ti_{0.22}O_4$ particles were prepared by adding $C_{18}H_{36}O_4Ti$ (0.1 M) to the LMO solution (the same solution as prepared above), and Ti–S multi-substituted $LiMn_{1.78}Ti_{0.22}O_{3.97}S_{0.03}$ particles were prepared by adding $C_{18}H_{36}O_4Ti$ and $(NH_4)_2S$ to the LMO solution. The reaction solution contained Li, Mn, Ti, and S sources before polymerization was started at 120 °C. The molar (M) ratio of Li : Mn : Ti was 1 : 2 : 0.3, whereas that of Li : Mn : Ti : S was 1 : 2 : 0.3 : 0.1. The subsequent synthesis was performed in the same sequence as in the LMO particle preparation. Based on previous research, in this study, O was substituted at the molar ratio of 0.03[6,26,31–34] and Mn ions were substituted below the molar ratio of 0.3.[15,35,36] Electrochemical tests were performed on two different concentrations of cations (Ti (at%)), and experiments were continued on the concentration that showed the best electrochemical results. Although the electrochemical results were similar, Ti-0.22 and S-0.03 cathodes were found to be optimal. The test results for the other cathodes are provided in the ESI† (Fig. S2). After substitution, the $LiMn_{1.8}Ti_{0.22}O_4$ and $LiMn_{1.78}Ti_{0.22}O_{3.97}S_{0.03}$ particles were denoted as LMTO and LMTOS, respectively (Table 1). A schematic illustration of the particle preparation is shown in Fig. 1.

Table 1 Physical parameter of LMO, LMTO, and LMTOS particles

Sample	Composition	a (Å)	V (Å^3)	Mn^{3+}/Mn^{4+}
LMO	$LiMn_2O_4$	8.221	555	0.83
LMTO	$LiMn_{1.78}Ti_{0.22}O_4$	8.236	558	1.15
LMTOS	$LiMn_{1.78}Ti_{0.22}O_{3.97}S_{0.03}$	8.238	559	1.15

Characterization of cathodes

The structures and morphologies of LMO, LMTO, and LMTS nanoparticles were characterized by performing FE-SEM (JSM-6701F, JEOL), energy dispersive spectrometry (EDS; Ultim@-MAX, OXFORD Instrument, UK), and XRD (Miniflex, Rigaku; Cu Kα 1.5406 nm as radiation source) in the 2θ range of 10°–90° with CuKα radiation at 20 kV. The particle size distribution was determined using the ImageJ software. XRD Rietveld refinement was performed using Fullprof Suite 2020. The crystal structures were examined using VESTA software. The microstructures and surface morphologies of the particles were analyzed by using HR-TEM (JEOL JEM-2100F TEM (200 kV)). Selected-area electron diffraction (SAED) was used to study the crystallinity and structure of the particles. XPS was performed by using a Kratos Axis Ultra spectrometer to determine the balance states of the ions. The spectra for −5 to 1195 eV were recorded with the pass energy of 187.35 eV and the step-width of 1.6 eV. The enlarged spectra in the Li 1s, Mn 2p, Mn 3p, Ti 2p, O 1s, S 2p, and C 1s regions were recorded with the pass energy of 20 eV and the step width of 0.125 eV. Fitting was performed using the XPSPEAK41 software. The electrochemical performance was evaluated by using two-electrode coin cells (CR 2032) and the Li metal foil as the counter and reference electrodes. To prepare the working electrodes, slurries of the cathodes were prepared by mixing a 70 wt% active material, 13% conductive carbon black (Imerys's Ensaco 350P, Yeoksam-dong, Gangnam-gu, Seoul), and 17% binder (polyvinylidene fluoride, PVdF) in an N-methyl pyrrolidone solvent, and the obtained slurry was coated onto an Al-foil current collector by employing the casting method. The coated slurry was dried at 110 °C for 15 h, and the electrode disks were punched after pressing at 8 kPa. A microporous polypropylene membrane was used as the separator, and a 1 M solution of $LiPF_6$ in EC : DEC (1 : 1, vol%) was used as the electrolyte. Galvanostatic charge–discharge tests (GCC test) (WDCS3000s, Won A-Tech, Yeogsam2-Dong, Kangnam-Ku Seoul Republic of Korea) was performed at current rates of 0.2–5C (theoretical capacity of 1C is 148 mA h g^{-1}) in a voltage range of 4.3–3.1 V to investigate the electrochemical properties of the cathodes. Cyclic voltammetry (CV) analyses were conducted using a Gamry Instrument (ZIVELAB, Seoul, Korea) with a potential range of 4.3–3.1 V (*vs.* Li^+/Li) and scan rates of 0.025, 0.07, 0.15, and 0.30 mV s^{-1}. The dynamic process of discharge/charge transformation in lithiation/delithiation was conducted *via* electrochemical impedance spectroscopy (EIS) in the frequency range of 0.1–1 MHz with a cutoff voltage of Open Circuit Potential (OCP) after 10 cycles of

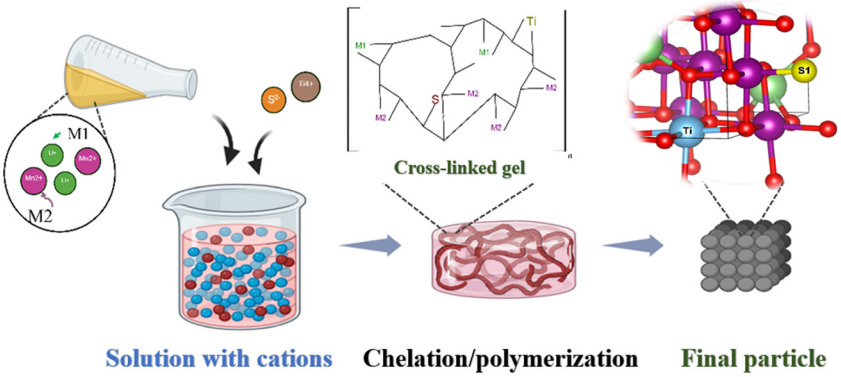

Fig. 1 Schematic illustrations of particle preparation.

GCC test at 10C. Throughout our research, we employed a 2-electrode configuration within a 2032-type coin cell for EIS measurements. Despite challenges in consolidating the sum of contributions from both the cathode and anode in this setup, we believe that the meaningfulness of the results can be compared by testing the cathode under identical conditions.

Results and discussion

Characterization of cathodes

EDS analysis was performed to determine the composition and elemental distribution of the particles, and Fig. 2 shows the EDS profile and elemental mapping. All three particles are composed of O and Mn. Ti is additionally observed for the LMTO particles, whereas Ti and S are observed for the LMTOS particles. The elemental content was calculated by using the atomic weight ratio in the EDS analysis (Table 1). Element mapping shows that each element has a uniformly distributed composition. Fig. 3 depicts the FE-SEM images of all particles. All three samples exhibit an octahedral morphology comprising nanosized particles, with dimensions of 139–342 nm for LMO, 151–763 nm for LMTO, and 199–915 nm for LMTOS (Fig. 3(d)). The LMTO particle shows a morphology similar to that of the LMO (average particle size of 250 nm) particle but with a slightly larger average particle size, estimated to be approximately 475 nm owing to the substitution with Ti, which has a larger atomic radius (Ti^{4+} (0.061 Å) > Mn^{4+} (0.053 Å)) (Fig. 3(b)). Single Ti substitution at approximately 0.22% atomic percentage (at%) shows no significant alteration in the net compound morphology. By contrast, the LMTOS particle exhibits a slightly more developed multifaceted morphology in the (111) and (001) planes within the same octahedral structure with an increased average particle size of approximately 530 nm, attributed to the multi-substitution of Ti and S. The atomic radii of Ti and S ions (0.184 nm) are larger than those of Mn^{4+} and O^{2-} (0.140 nm) and cause the broadening effect of the partial deformation of the MnO_6 octahedra.[30,37] The (001) plane is expected to have a denser arrangement of Li^+ than the (111) plane does in spinel $LiMn_2O_4$ primarily because the (001) plane is a close-packed plane with closely packed atoms. Enhancing these aspects would yield greater benefits for boosting Li^+ transport kinetics.[38] Hence, similar to previous results, individual Ti or S substitutions in small quantities do not significantly alter the surface,[6,7] except for a minor augmentation in the dominance of the (111) and (001) planes in the LMTOS particle, and the particles share a similar morphology. The structural features were further analyzed by using XRD, XPS, and HR-TEM. Fig. 4(a)–(f) present HR-TEM images of the particles. The HR-TEM results show that all three particles have an octahedral shape with a single-crystal structure (Fig. 4(a)), which is in good agreement with the FE-SEM results. The SAED results of the LMTO particles show a well-ordered single-crystal structure, which indicates that Ti ions are homogeneously distributed in the spinel LMO structure and no impurity phase is present in the LMTO particle (Fig. 4(c) and (d)). The LMTOS particle exhibits a homogeneous distribution of Ti and S from the bulk to the surface (Fig. 4(f)). In addition, compared with those of the LMO and LMTO particles, the HR-TEM results of the LMTOS particle show that the multifaceted (111) and (001) planes are slightly developed. For all three particles, the lattice spacing is approximately 0.48 nm, which is in accordance with the (111) crystal plane of spinel $LiMn_2O_4$. The crystal structures of the particles were characterized by using XRD, and the patterns are shown in Fig. 5(a) and (b). All three particles display only the characteristic diffraction peaks for a well-crystallized spinel phase with the $Fd\bar{3}m$ cubic space group. The corresponding lattice parameter (a), computed by performing Rietveld refinements (Fig. 5(b)), is given presented Table 1. According to the XRD results, the lattice parameters of the Ti-substituted LMTO particle and the Ti- and S-substituted particles are slightly higher than that of the LMO particle. The (220) peak located at $2\theta \approx 30.7^\circ$ in the XRD patterns represents the tetrahedral site (8a), and the (220) peak is not detected for all particles. This shows that the tetrahedral sites (8a) are only occupied by Li^+, which exhibits undetectable (220) signals owing to their very low X-ray scattering ability.[17] Therefore, for the LMTO particle, Mn^{4+} is partially substituted with Ti^{4+}, having a larger ionic radius, at the octahedral 16d site,[16] which can be attributed to the slightly increased lattice parameter. The lattice parameter for the LMTOS particle is higher than those of the LMO and LMTO particles because the ionic radius

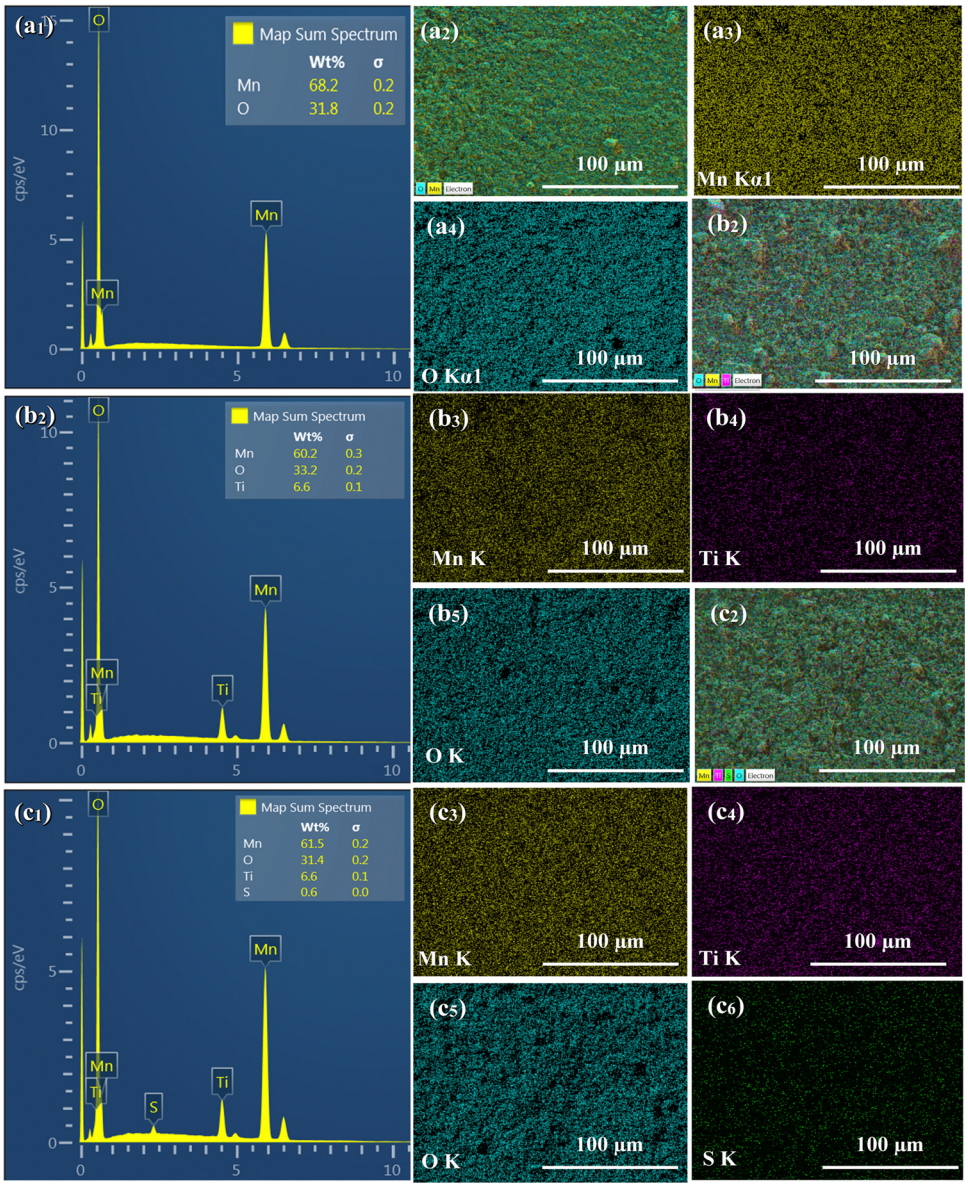

Fig. 2 FE-SEM with EDS results of (a1) LMO, (b1) LMTO, and (c1) LMTOS particles. EDS mapping results: (a_1) LMO, (b_1) LMTO, and (c_1) LMTOS (Mn ((a_2), (b_2), and (c_2)); Ti ((b_3) and (c_3)); O ((a_3), (b_4); and (c_4)); and S (c_5)).

of S^{2-} (1.84 Å) is larger than that of O^{2-} (1.40 Å).[6] Fig. 5(c) and Fig. S3(a) (ESI†) present schematic representations of the crystalline structures of cubic spinel $LiMn_2O_4$ and the synthesized LMTOS, respectively, showing the spatial arrangement of the atoms. All synthesized particles adhere to the $Fd\bar{3}m$ space group of the spinel structure. In the cubic spinel $LiMn_2O_4$ crystal structure, Li and Mn ions strategically occupy the tetrahedral 8a sites and octahedral 16d sites, respectively, whereas O ions reside at the 32e sites, as depicted in Fig. S3(a) (ESI†). Li^+ diffusion in this spinel structure occurs by hopping between the 8a tetrahedral sites, facilitated by the 16c octahedral sites.[39] The introduction of Ti and S into the $LiMn_2O_4$ structure is expected to modify the bonding characteristics and crystal size within the lattice, as revealed by the XRD pattern of the synthesized LMTOS crystal structure (Fig. 5(c)). In the schematic representation of the crystalline structure, Ti1 occupies the octahedral 16d sites, replacing Mn, whereas S replaces O and is located at the 32e site. Li remains situated at the tetrahedral 8a sites. Thus, the arrangement of atoms, except for Li^+, can change randomly, forming new chemical bonds. In the $LiMn_2O_4$ crystal structure, Li–O and Mn–O bonds are evident. With the substitution of Ti and S, additional types of chemical bonds, including Mn–O, Ti–O, Li–O, and Li–S bonds, are formed in the LMTOS crystal structure. The movement of Li^+ within this spatial framework is influenced by the bonding energy between the Li ions and surrounding atoms.[39,40] Therefore, as previously explained, alterations in the bonding characteristics and crystal lattice can affect the structural stability, electronic conductivity, and electrochemical performance of the materials. For furthermore investigations of XRD

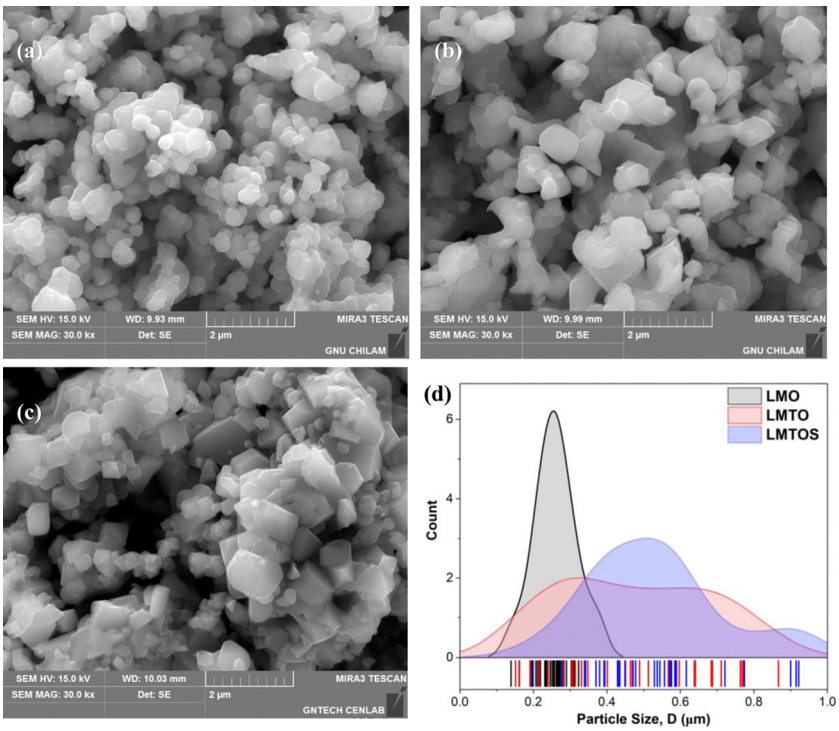

Fig. 3 FE-SEM surface images of (a) LMO, (b) LMTO, (c) LMTOS particles (scale bar in all images: 2 µm), and (d) particle-size distribution for three synthesized particles. LMO, LMTO, and LMTOS are depicted by the black, red, and blue curves, respectively.

patterns, the crystal facet XRD patterns of spinel $LiMn_2O_4$ offer valuable insights into the crystal structure and orientation of the material through intensity ratios: $I_{(111)}/I_{(311)}$ and $I_{(400)}/I_{(111)}$ (Fig. S3(b), ESI†). Specifically, the $I_{(111)}/I_{(311)}$ ratio indicated the growth of the (111) crystal plane, whereas the (400) crystal facets corresponded to the (001) crystal planes.[41] The ratio of $I_{(111)}/I_{(311)}$ was the highest in the LMO (1.73) particle, indicating a preferential orientation along the (111) crystallographic direction.[41–44] This value decreased slightly in the LMTO (1.25) particle and was the lowest in the LMTOS (1.15) particle. In contrast, the (001) plane was slightly developed in the LMTO particle, confirming a reduced intensity ratio of $I_{(111)}/I_{(311)}$ and $I_{(400)}/I_{(111)}$ intensity ratios of LMO; however, the FE-SEM and HR-TEM results indicated that it was relatively small and not visible. However, it is hypothesized that the presence of this invisible (001) plane can positively affect the electrochemical C-rate performance of the LMTOS particles. For the LMTOS particles, the lowest (111) plane predominance decreased significantly, and the $I_{(400)}/I_{(111)}$ ratio increased, indicating an increased (001) plane, which is consistent with the FE-SEM and HR-TEM results, proving that even a small amount of visible change occurred. The prevalence of the (001) crystal plane suggests enhanced support for the Li^+ transport kinetics, which in turn could significantly improve the C-rate performance of the materials.[38] Furthermore, the compositions of the particles and the chemical states of the Mn, Ti, and S ions were investigated using XPS analysis, Fig. 6. For all three particles, the energy band at approximately 52 eV was assigned to Mn 3p and Li 1s, the band at approximately 533 eV to O 1s, and the bands at approximately 641 and 653 eV to Mn $2p_{3/2}$ and Mn $2p_{1/2}$, respectively (Fig. 6(a)).[17] Ti $2p_{1/2}$ and $2p_{3/2}$ peaks at approximately 457.2 and 462.7 eV is visible to confirm the presence of the Ti element in both LMTO and LMTOS particles, in agreement with the EDS analysis, Fig. 6(a) and (b). The binding energy splitting between $2p_{3/2}$ and $2p_{1/2}$ is about 5.5 eV, indicating that Ti is a tetravalent oxidation state for both LMTO and LMTOS.[15,16] For LMTOS only, the detection of peaks at the core levels of S $2p_{1/2}$ (162.4 eV) and S $2p_{3/2}$ (161.4 eV) indicates that the substituted S has partially substituted the O sites to form the new bond Mn–S and possesses the state of S^{2-}, which can make the spinel structure more stable (Fig. 6(c)).[6] The deconvoluted results in Fig. 6(d) show the distinct differences between the particles in the Mn 2p spectra. The Mn $2p_{3/2}$ and Mn $2p_{1/2}$ curves fit the two peaks at approximately 642 and 641 eV, and 653 and 651 eV, corresponding to Mn^{3+} and Mn^{4+}. For the LMTO and LMTOS particles, the Mn2p peaks were similar and shifted to lower binding energies than the LMO particles; and the contents of Mn^{3+} and Mn^{4+} are 45.55%, and 54.45% for LMO, 53.46%, and 46.54% for LMTO, 53.40% and 46.6% for LMTOS, respectively.[45] The substitution of Ti^{4+} ions increased the Mn^{3+}/Mn^{4+} ratio for the LMTO and LMTOS particles, indicating that Ti^{4+} substituted the Mn^{4+} sites in the bulk crystal structure.[15,17] An increase in the ratio of Mn^{3+}/Mn^{4+} ions by Ti^{4+} substitution is one of the factors that changes the lattice parameters, and the result is in good agreement with the XRD patterns. Fig. 6(e) shows the O 1s fine spectrum, the O 1s spectrum for three particles exhibits two discernible oxygen components identified as O lattice (529.5 eV) and O non-lattice (531.6 eV).[46–49] These peaks are associated with lattice oxygen within metal–oxygen bonds and defective or adsorptive oxygen

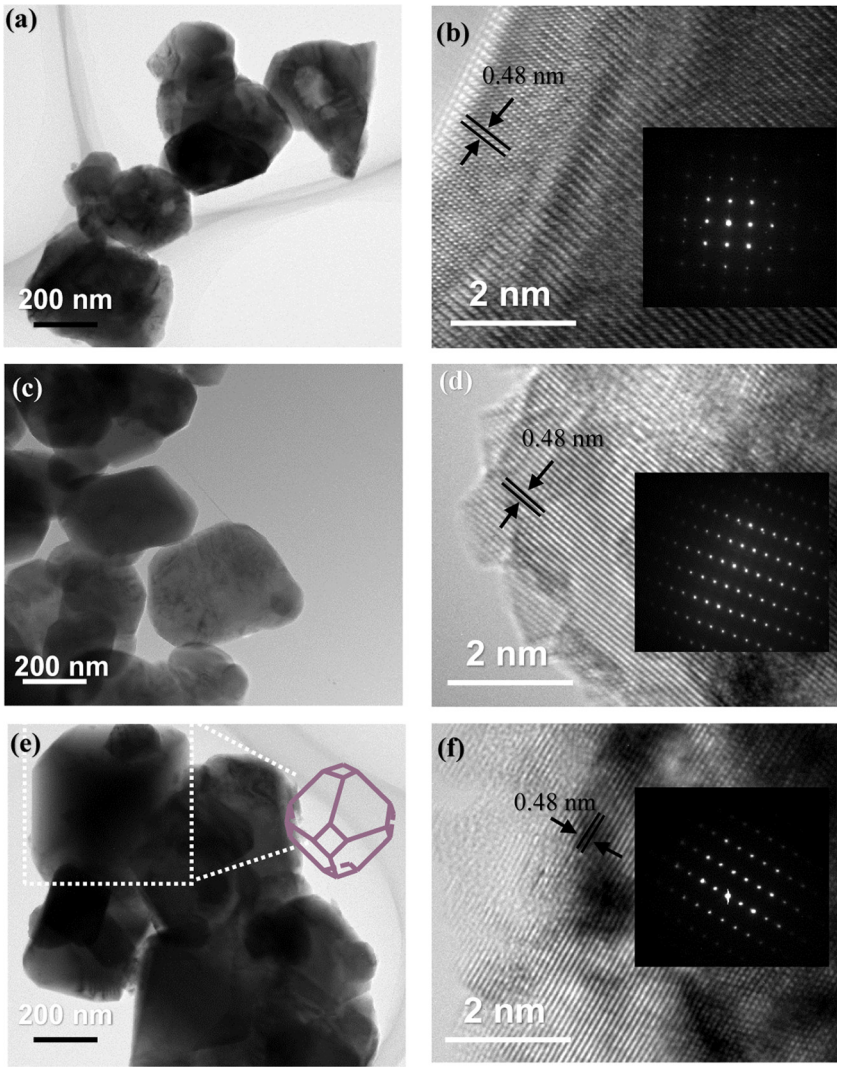

Fig. 4 HR-TEM images of (a) and (b) LMO, (c) and (d) LMTO, and (d) and (f) LMTOS (scale bar: 200 nm and 2 nm), and the inset shows the corresponding SAED pattern (region shown in (b) LMO, (d) LMTO and (f) LMTOS particles).

species, respectively. Considering a baseline O 1s peak area of 100% for LMO, LMTOS exhibited a 1.8% reduction, while LMTO displayed a 0.3% decrease. Particularly noteworthy is the observation that the O 1s peak area in the LMTOS particle is the lowest among the particles. This divergence could be ascribed to the possible mitigation of oxygen defects through S substitution. According to the comprehensive characterization described above and previously reported in the literature, Ti(IV) partially substitutes Mn(IV) on octahedral 16d, S partially substitutes O on the 32e side of the crystal structure of spinel $LiMn_2O_4$[50] and it can be written that the structure of the substituted particles can be written as $Li(Mn^{3+}Mn^{4+}_{2-x}Ti_x)O_4$ and $Li(Mn^{3+}Mn^{4+}_{2-x}Ti_x)O_{4-y}S_y$. The substitution of Ti(IV) and multi-substitution of Ti(IV) and S(II) in the bulk structure did not disturb the spinel crystalline structure and morphology but slightly increased the lattice parameters and ratio of Mn^{3+}/Mn^{4+} ions, which are factors affecting the electrochemical properties. For LMTOS particles with small amounts of S(II) substitution, the multifaceted morphologies of the (111) and (001) planes develop slightly, which leads to the positive effect of producing higher ionic and electronic conductivities than only Ti(IV)-substituted particles.

Electrochemical properties

In Fig. 7(a), CV results of the cathodes (2nd cycle) are shown, with experiments conducted at a scan rate of 0.2 mV s^{-1} within a potential range of 3.1 to 4.3 V. The CV redox peak potential difference (ΔE_p) for three cathode configurations, emphasizing distinct redox peaks, is assessed in Fig. 7(b). The features of the redox peaks provide valuable information on the kinetics of Li^+ insertion/extraction in electrochemical reactions. A sharp and well-defined peak is indicative of rapid Li^+ insertion/extraction kinetics, whereas a low redox potential difference indicates several favorable characteristics of the electrochemical behavior of a cathode material, such as reduced voltage hysteresis and less polarization.[51] CV results were similar in curve shape for the three cathodes, with two well-separated reversible plateaus around 4.05 V and 4.18 V corresponding to a two-step Li^+ extraction/insertion from/into the spinel phase: the

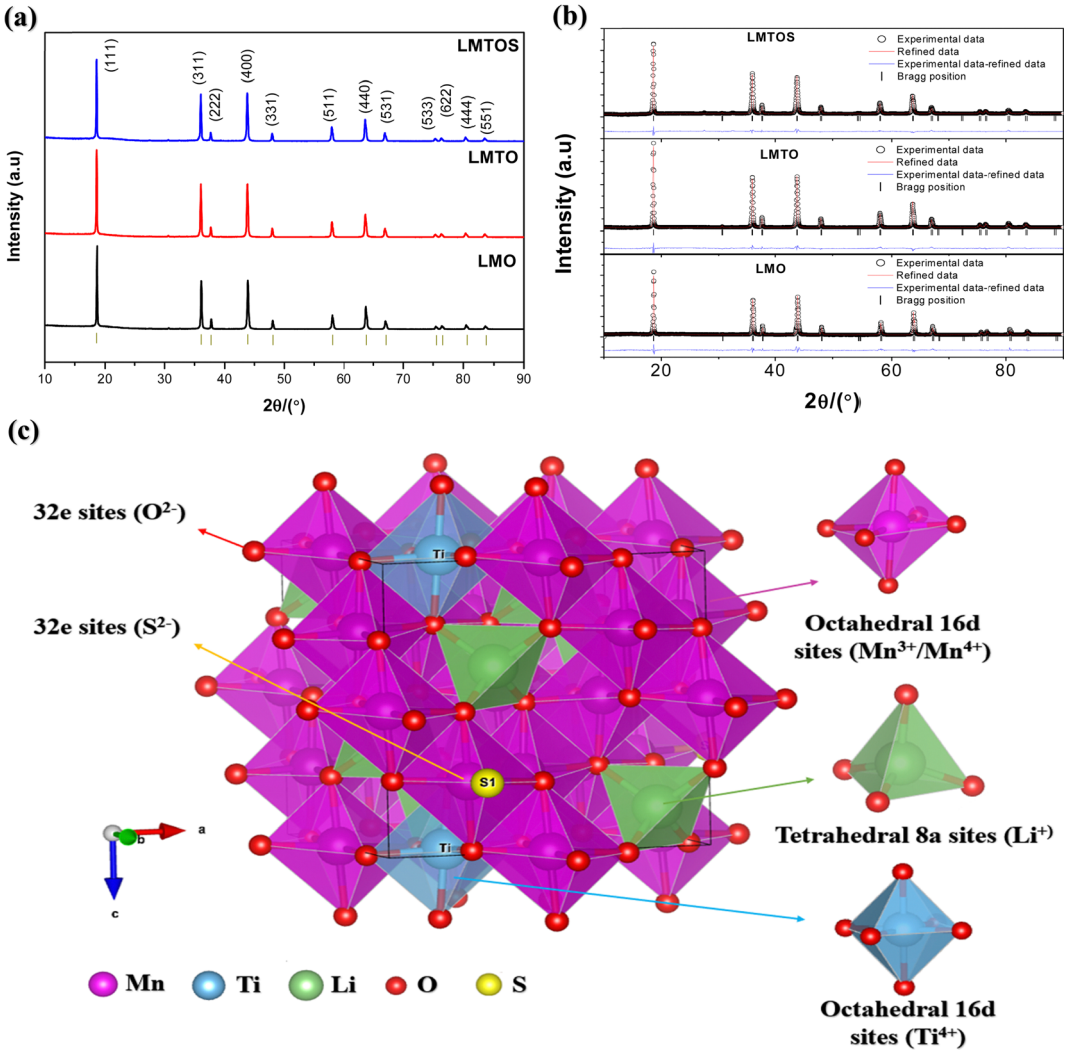

Fig. 5 (a) XRD patterns of particles, and JCPDS data for a cubic spinel structure (*Fd*$\bar{3}$*m*, space group 227; JCPDS data No. 35-0782) are shown in black (bottom). Black, red, and blue spectra represent the synthesized LMO, LMTO, and LMTOS particles. (b) Rietveld refinement of samples, experimental data (empty red circles), and corresponding profile computed by performing Rietveld refinement (black solid line) based on the cubic spinel structures and their differences; the Bragg positions (blue solid line) are shown below each pattern. (c) Schematic representation of the crystalline structure of Ti- and S-substituted LMTOS particle, showcasing the unit cell with atomic bonds and metal sites. Mn1 and Ti1 positioned at 16d is denoted by a pink and blue atom, respectively, Li1 at 8a is represented by a green atom, and O and S is indicated by small red and yellow atoms, respectively, providing insight into the cubic-spinel LMTOS crystal structure.

first step can be expressed as $LiMn_2O_4 \rightarrow Li_{(1-x)}Mn_2O_4 + xLi^+ + 0.5e^-$ ($x < 0.5$), and the second as $Li_{(1-x)}Mn_2O_4 \rightarrow 2MnO_2 + (1-x)Li^+ + (1-x)0.5e^-$ ($x > 0.5$) is a fully delithiated system (MnO_2).[29] Comparing the three cathodes reveals that the intensity of the peak couples gradually decreased from the LMO cathode to the LMTOS and LMTO cathodes, and the voltage separation of each redox peak increased, which is related to the size of the particles. Because of the smaller particle size, the LMO cathode exhibited sharper peak intensities and lower polarization than the LMTO and LMTOS cathodes because of the higher electrochemical activity owing to the larger specific surface area.[29] From result Fig. 7(b), the larger redox peak difference in LMO cathode of 0.16 V (redox – 1) and 0.17 V (redox – 2) suggests potential challenges, possibly related to irreversible processes during cycling (Fig. 7(b)). The introduction of Ti into $LiMn_2O_4$ results in a diminished redox peak difference of LMTO cathode (0.08 V and 0.07 V for redox – 1 and redox – 2), indicating an alteration in electrochemical behavior marked by reduced voltage hysteresis, less polarization and enhanced reversibility. LMTOS cathode further reduces the redox peak difference (0.06 V and 0.07 V for redox – 1 and redox – 2), suggesting a synergistic effect of Ti and S multi-substitution. This results in a lower voltage hysteresis and aligns with improved crystal stability can be observed in the potential for enhanced stability during charge–discharge cycles. Fig. S4(a)–(f) (ESI†) show the CV of the cathodes at different scan rates (0.025–0.3 mV s^{-1}) within a potential range of 3.1 to 4.3 V. Based on the curves recorded at different scan rates for three cathodes, the diffusion coefficient of Li^+ ions (D_{Li}) can be calculated using the Randles–Sevcik equation. D_{Li} was calculated from the dependence of

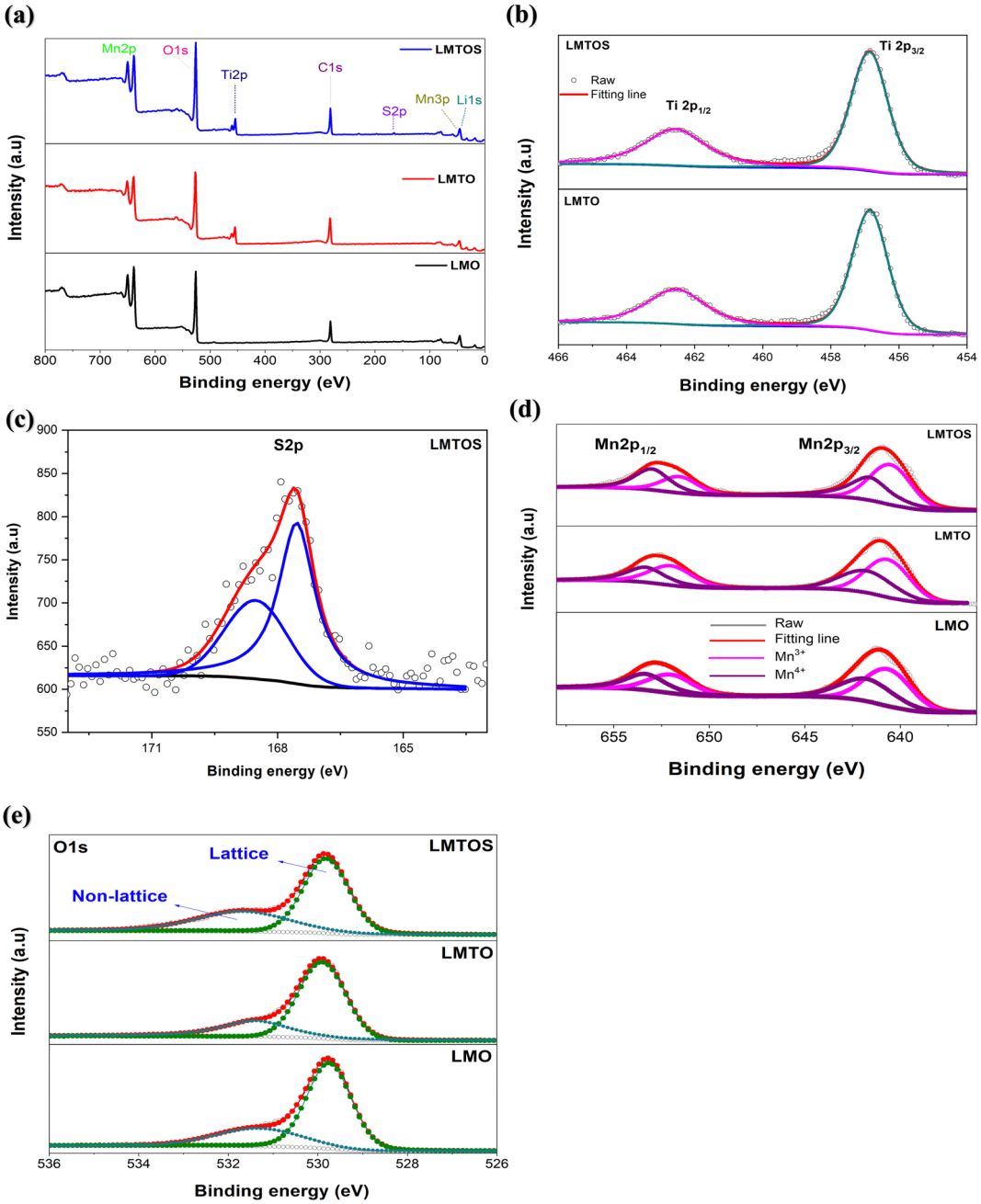

Fig. 6 XPS spectra for particles: (a) full spectra, (b) Ti 2p, (c) S 2p, (d) deconvoluted profiles of Mn $2p_{3/2}$ and (e) the O 1s XPS spectrum.

the peak current density on the square root of the scan rate (Fig. 7), expressed as:[38]

$$I_p = (2.69 \times 10^5) n^{\frac{3}{2}} A D_{Li}^{\frac{1}{2}} \nu^{\frac{1}{2}} C_{Li}, \quad (2)$$

where I_p is the peak current (A), n is the electron transfer number (n = 1), A is the surface area of the electrode (cm^2), D is the apparent diffusion coefficient of Li^+ ($cm^2\ s^{-1}$), ν is the voltage scanning rate ($V\ s^{-1}$), and C_{Li} is the concentration of Li^+ ($mol\ cm^{-3}$). The mean Li^+ diffusion coefficients of the cathodes were calculated (Table S1, ESI†) to be the highest value of $8.1 \times 10^{-10}\ cm^2\ s^{-1}$ for the LMO cathode, $6.4 \times 10^{-10}\ cm^2\ s^{-1}$ for the LMTO cathode, and $7.9 \times 10^{-10}\ cm^2\ s^{-1}$ for the LMTOS cathode, confirming similar values to the previously reported substituted and non-substituted $LiMn_2O_4$ cathodes.[32,38] As reported, the diffusion kinetics of Li^+ diffusion vary highly depending on factors such as the transport length and number of accessible sites on the surface of active materials, surface area,[52,53] and morphology. It was concluded that the LMO cathode showed a higher Li^+ diffusion coefficient owing to the higher surface area due to the smaller particle size. LMTO and LMTOS have larger particle sizes and lower average diffusion coefficients than the LMO cathodes. It has been reported that substituting a certain amount of Mn ions with Ti ions improves the Li^+ diffusion

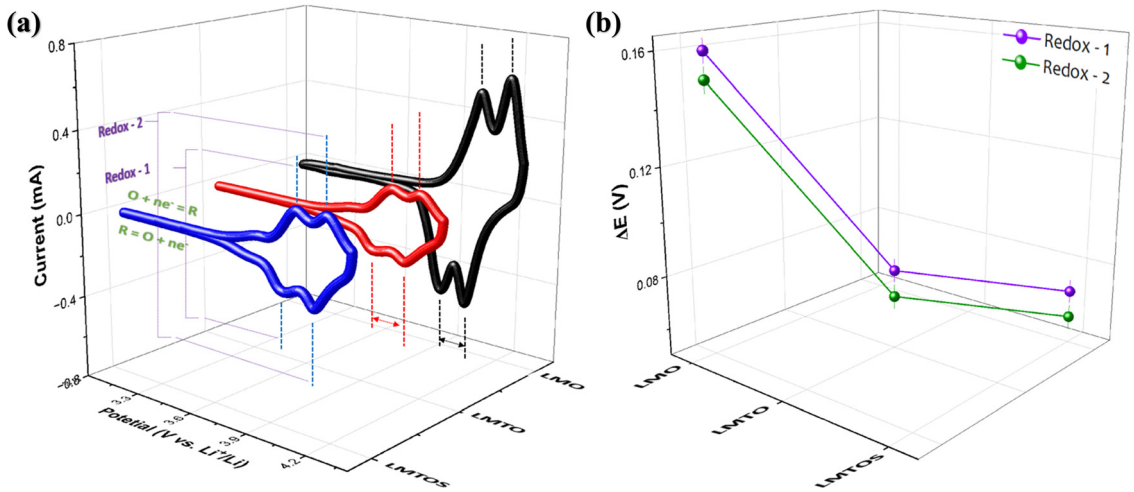

Fig. 7 (a) CV results of the cathodes, with experiments conducted at a scan rate of 0.2 mV s^{-1} within a potential range of 3.1–4.3 V. (b) CV redox peak potential difference (ΔE_p) for three cathode configurations, emphasizing distinct redox peaks.

coefficient.[15] In our case, it was not possible to explain the effect of Ti ion substitution based on the difference in the active surface area, but it was possible to compare the results of the LMTO and LMTOS cathodes with similar particle sizes. For the two substituted cathodes, although the LMTOS cathode has a larger particle size than LMTO, the LMTOS cathode shows a slightly higher Li^+ diffusion coefficient than the LMTO cathode, which proves that Ti and S have a synergistic effect on the physical parameters of spinel $LiMn_2O_4$. The increased ion diffusion coefficient due to the synergistic effect of Ti and S can be explained as follows: (1) the larger cell parameter caused by the expansion of the lattice arising from the larger-anion Ti and S substitutions is favorable for facilitating the Li^+ transport kinetics; (2) a larger cell parameter enables the tilting of the M–O_6 octahedron, which can reduce the migration resistance of Li^+;[17,54] (3) the Ti–O bond is stronger than the Mn–O bond, which indicates a weaker Li–O bond and Li^+ easily migrates from the Li–O bond.[17] On the S side, easy Li^+ intercalation and extraction are expected because of the expansion of the lattice arising from the larger anion substitution and lower bond dissociation energy of Li–S than that of Li–O;[20] (4) this increased substitution strength helps to stabilize the crystal structure framework and reduce structural transformations because of stronger interatomic interactions within the crystal lattice; (5) the dominance of the (111) and (001) planes on the surface is more favorable for facilitating Li^+ transport kinetics, and slight variations in the LMTOS morphology may aid Li^+ diffusion.[38] The electrochemical performances of the three cathodes cycled between 4.3 V and 3.1 V at 25 °C are compared in Fig. 8(a)–(e). Fig. 8(a)–(c) show the 1st, 50th, and 100th charge/discharge curves for all three cathodes cycled at 1C. Two plateaus appear in the charge/discharge curves for all three cathodes and can be readily assigned to a one-phase transition reaction at 3.9 V and a two-phase transition reaction at 4.1 V.[29] Despite the less well-defined plateaus of LMTOS, the LMTO and LMTOS cathodes exhibit similar charge/discharge profiles, but their electrochemical behaviors are different from the typical ones of spinel LMO. The variations in the plateau shape highlight the enhanced structural stability of LMO and are attributed to subtle alterations in the chemical bond forces within its structure. The initial charge/discharge capacities of all cathodes are similar: 141/135, 139/134, and 139/136 mA h g^{-1} for LMO, LMTO, and LMTOS, with corresponding Coulombic efficiencies being 95.5%, 96.5%, and 97.2%, respectively. For all cathodes, the Coulombic efficiency initially decreases to material dissolution and side reactions,[29,55,56] but from the fifth cycle, the Coulombic efficiency increases with the cycle stabilization, reaching 99.6%, 99.2%, and 99.2% for LMO, LMTO, and LMTOS, respectively. The LMO cathode exhibits a relatively low initial Coulombic efficiency than LMTO and LMTOS do. The size and stabilized structure of the particles can also play a role. The smaller particle size and larger specific surface area of LMO can lead to greater Mn dissolution. By contrast for specific surface area, the LMTO and LMTOS cathodes are higher than that of LMO, indicating that a substituted structure can suppress irreversible reactions (such as the deposition of electrolyte decomposition products) and maintain the stabilized structure.[17] In both substituted cases, LMTOS possesses a higher initial Coulombic efficiency (97.15%) than LMTO. This enhanced electrochemical reversibility behavior can be related to the synergistic effect of Ti and S, as mentioned previously. The LMO cathode exhibits poor cycling performance, but the capacity retention is significantly improved for both substituted cathodes. After 500 cycles are completed, the charge/discharge capacities of LMO and LMTO are 46/46 and 103/103 mA h g^{-1}, respectively, whereas LMTOS exhibits excellent cycling performance and achieves a charge/discharge capacity of 123/122 mA h g^{-1}. The corresponding capacity retentions are 33.9% for LMO, 76.6% for LMTO, and an impressive 90.3% for LMTOS. For the LMTO cathode, cycling performance is enhanced because of the presence of the tetravalent valence Ti cation, which stabilizes the spinel framework. This stabilization leads to an expansion in the unit cell volume, promoting the diffusion of Li^+ and increasing the intercalation voltage.[57] In addition, Ti substitution in $LiMn_2O_4$ helps reduce oxygen release

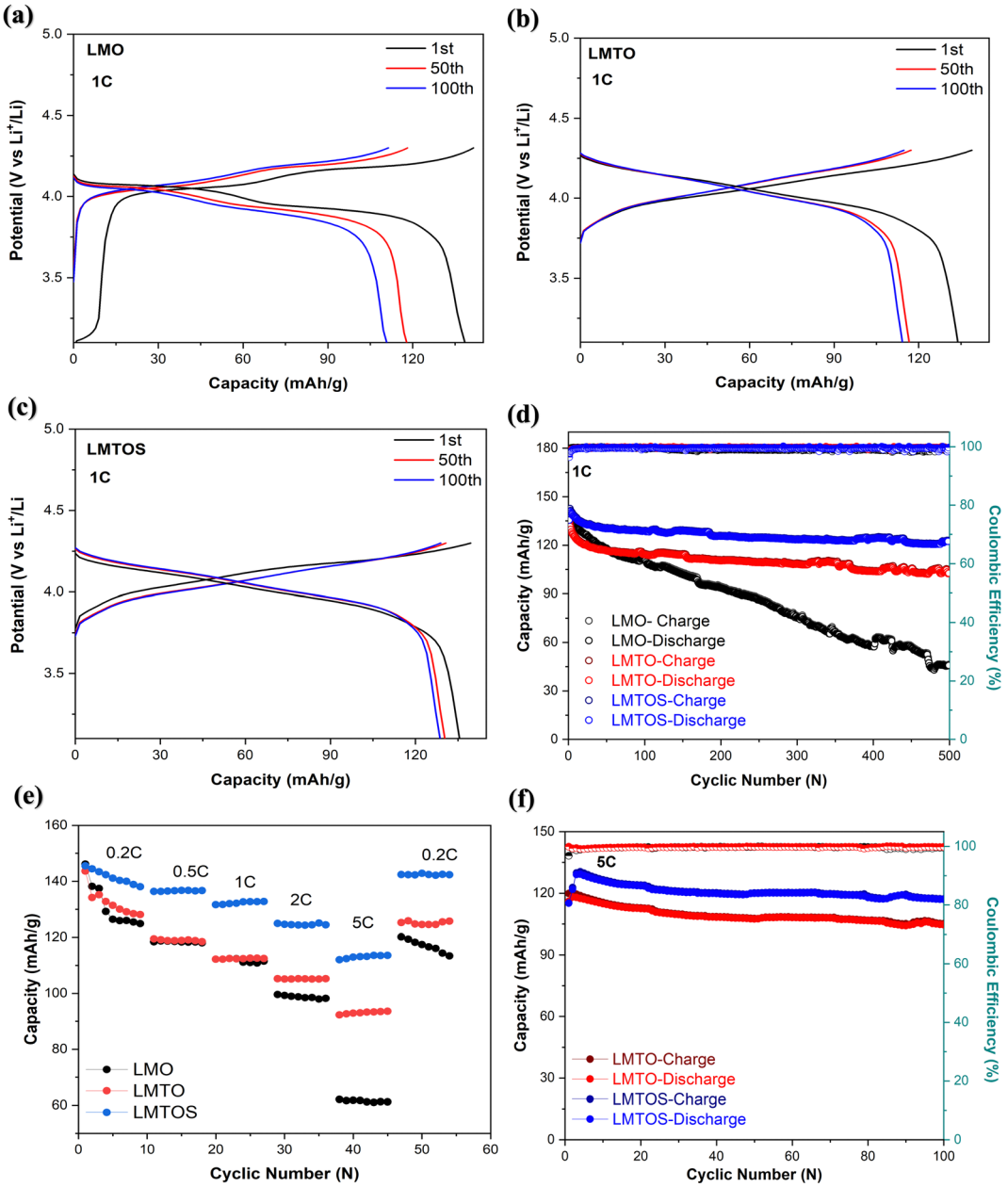

Fig. 8 Charge/discharge capacity profile of (a) LMO, (b) LMTO, and (c) LMTOS cathodes and (d) charge/discharge cycling performance of the three samples at cut-off voltages of 4.3–3.1 V (1C). (e) Rate performance of three cathodes from 4.3 to 3.1 V at different current densities, and (f) charge/discharge cycling performance of three cathodes at cut-off voltages of 4.3–3.1 V (5C).

during LIB charging and discharging, thereby addressing safety concerns and promoting cycling efficiency.[38] The most significant improvement in the electrochemical performance of LMTOS reveals that the substitution of both Ti and S in the spinel LMO cathode material can result in an even greater improvement in cycling performance compared with when only Ti is substituted. The combination of Ti and S multisubstitution in LMO creates synergistic effects. The rate performances of all the cathodes are shown in Fig. 8(e) and (f). The substituted cathodes show very high rate performance, and at a high rate capability, the capacity drops significantly in the LMO cathode. For all three cathodes, the capacity decreases momentarily at high current densities with an increase in the proportion of the side reaction as a direct consequence of the Bulter–Volmer equation, resulting in a nonreversible reaction.[58,59] After the high rate (5C), the capacity recovery at the fundamental cycle rate of 0.2C indicates that the crystal structure is preserved. Further, the discharge capacities after 10 cycles at each C rate are 128, 119, 113, 105, 93, and 126 mA h g^{-1} for LMTO and 140, 138, 133, 125, 115, and 142 mA h g^{-1} for LMTOS, which are the highest. Ti substitutions have been shown to improve the rate performance of spinel LMO, and our substituted cathodes yield similar results.[7,15,17] In the case of the multisubstitution with S and Ti, the presence of S enhances Li+ diffusion kinetics within

the electrode, facilitating faster Li^+ transport and higher rate capabilities.[60] To assess the cycling performance under high C-rate conditions, 100 cycles were executed at a rate of 5C (Fig. 8(f) and Fig. S5, ESI†). At the start, both LMTO and LMTOS exhibited an initial charge/discharge capacity of 120/116 mA h g^{-1} and 115/115 mA h g^{-1}, respectively. After 100 cycles, the capacities reached 105/105 and 117/117 mA h g^{-1} for LMTO and LMTOS, respectively. This both cathodes represent excellent a capacity retentions of 89.9% and 90.1% of the 3rd capacity, respectively. The C-rate results confirm that S's contribution of S, along with that of Ti, has a strong influence on the cycling performance, especially the improvement in the high-rate performance. EIS was performed to further investigate the reaction kinetics. Nyquist plots were obtained in the frequency range of 0.1 MHz to 1 MHz at OCP (V) (Fig. 9). To ensure that observed effects can be confidently ascribed to the substitution of elements rather than differences in electrode mass or thickness, the thickness of all experimental cathodes uniformly adjusted to approximately 12 μm, while maintaining an active mass loading of up to 1.51 ± 0.02 mg cm^{-2}. An equivalent circuit was employed to reproduce the experimentally obtained EIS spectra, as illustrated in the inset of Fig. 9(a). The components of this circuit include R_s, R_{ct}, CPE, and Z_w, which represent the solution resistance, charge-transfer resistance, constant phase element, and Warburg impedance, respectively, and characterize the electrode/electrolyte interface. The semicircle is usually attributed to the solution resistance (R_s) ranging from zero to the beginning of the semicircle, the combination of the solid/electrolyte interface film resistance (R_f) and charge transfer impedance (R_{ct}) in the high-frequency region at the electrode surface. The inclined line at low frequencies is described as a Warburg-type element, reflecting the solid-state diffusion of Li into the bulk of the active materials.[29,59,61] These are designated as the solid electrolyte interface impedance (R_f) and charge-transfer impedance (R_{ct}), which are typically associated with the electronic conductivity of the materials.[15,62] Fig. 9(a) illustrates that the solution resistances (R_s) are comparable, measuring 3.9 Ω, 4.1 Ω, and 3.9 Ω for the LMO, LMTO and LMTOS cathodes. This proposes consistent interactions between the cathode surfaces and the electrolyte, providing to homogeneous electrical properties and solution resistances. In terms of charge transfer resistance, the value for LMO (135 Ω) is larger than that for both substituted cathodes. The resistance in LMO increases because of the distortion of the crystal structure, whereas the Ti substitution and Ti and S multisubstitution result in a more stable crystal lattice and Li^+ diffusion channel and lower charge-transfer resistance. LMTOS exhibits the lowest resistance value of 86 Ω (LMTO exhibits 93 Ω), indicating that LMTOS has the lowest charge-transfer resistance and that S multi-substituted with Ti in spinel LMO improves the electron conductivity. To determine the Warburg factor (σ) and lithium-ion diffusion coefficient (D_{Li}), the real part resistance is plotted against the inverse square root of the angular frequency within the low-frequency range, as depicted in Fig. 9(b). The slope of this plot is utilized to derive the Warburg factor, and eqn (3)[63] is applied to calculate D_{Li}.

$$D_{Li} = \frac{R^2T^2}{2A^2n^4F^4C^2\sigma^2}, \quad (3)$$

where R is the gas constant (8.314 J mol^{-1} K^{-1}), T is the test absolute temperature (298 K), A is the surface area of the cathode, n is the number of transferred electron, F is the Faraday constant (96 500C mol^{-1}), C is the Li^+ concentration (1 mol L^{-1}, in the electrolyte), and σ is the Warburg coefficient, which is related to Z' (slope of the fitted $Z'/\omega^{-1/2}$ line).

In the calculations, σ and D_{Li} of the LMO cathode were determined to be 75.2 Ω cm^2 $S^{-1/2}$ and 9.9 × 10^{-10} cm^2 S^{-1}, respectively, and those of the LMTO and LMTOS cathodes were 128.0 Ω cm^2 $S^{-1/2}$ and 4.1 × 10^{-10} cm^2 S^{-1} and 88.8 Ω cm^2 $S^{-1/2}$ and 7.3 × 10^{-10} cm^2 S^{-1}, respectively. The results obtained from the CV tests and EIS analyses yielded similar values for D_{Li}. This agreement in the results provided a robust confirmation of the obtained D_{Li} values. Therefore, the substituted cathodes exhibited better cycling and rate performances than LMO. The contribution of S along with Ti led to improved structural stability, enhanced conductivity (both electronic and ionic), and improved Li^+ diffusion. This synergy results in batteries with significantly improved cycling performance compared with those resulting from single substitution or no substitution in LMO. Fig. 10 displays a comparison between the electrochemical properties of anion- and

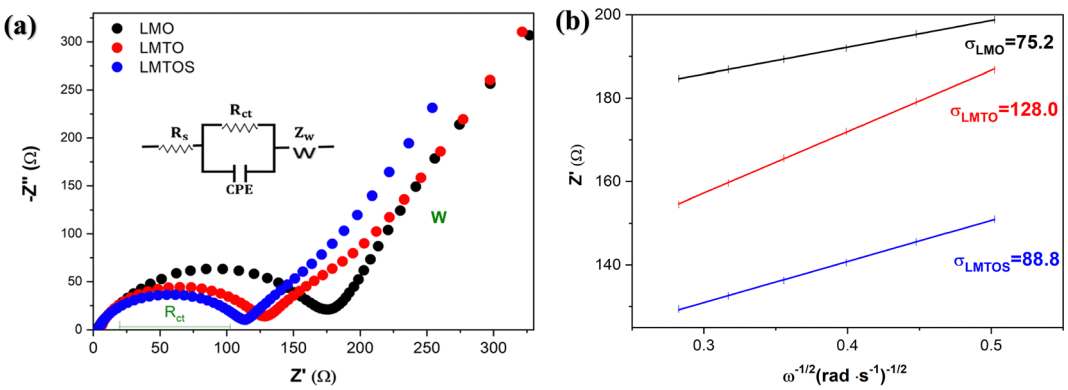

Fig. 9 EIS of the cathodes after 10 cycles of GCC test at 10C over a frequency range of 0.1–1 MHz at the OCP (V) state; (b) corresponding linear fitting curve of Z' *vs.* $\omega^{-1/2}$ at low frequencies.

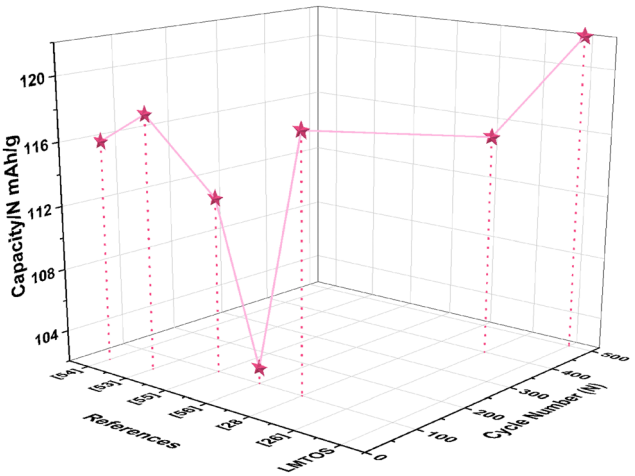

Fig. 10 Electrochemical properties of cathodes synthesized by using the sol–gel method compared with those synthesized under similar conditions by using the solid-state reaction methods.

cation-multi-substituted LMO cathodes synthesized under similar conditions by using the sol–gel method and solid-state reaction method. The comparative results encompass cathodes synthesized *via* the sol–gel method and tested at 0.5C for 40, 50, and 100 cycles[64–66] and those synthesized *via* the solid-state reaction method and assessed at 1C and 0.5C for 100 and 400 cycles.[28,30,67] As illustrated in the comparative graph, the LMTOS cathode demonstrates a notably higher discharge capacity, even after 500 cycles at a higher rate of 1C. This satisfactory cyclic performance not only aligns with but also exceeds the performance levels reported in prior research, thereby highlighting the enhanced electrochemical performance in terms of both cycling stability and rate performance. These findings underscore the enhanced performance of our multi-substituted materials, positioning them as promising candidates for advanced energy storage applications.

Conclusions

In this study, a new spinel LMTOS was obtained *via* substitution with Ti and S in spinel LMO by using the sol–gel method. The synergistic effect of Ti and S substitutions was studied and compared with effects of only Ti substitution and no substitution on LMO cathodes. The characterization results showed that Ti and S were successfully substituted into the spinel structure, and Ti^{4+} replaced Mn^{4+} and S^{2-} replaced O^{2-} at the octahedral 16d and 32e sites, respectively. Ti substitution had no significant effect on morphology and crystal structure, except for the lattice parameters of the sample. By contrast, Ti and S substitutions had no significant effect on the crystal structure but slightly affected the surface morphology by affecting the growth rate of the (001) crystal faces and the lattice parameters. The electrochemical performances of the substituted cathodes were evaluated in terms of cycling performance and rate capability. The results demonstrated that Ti-substituted LMO exhibited improved cycling performance compared with non-substituted LMO and achieved a 10th discharge capacity of 93 mA h g^{-1} (5C) in rate capability and a charge/discharge capacity of 103/103 mA h g^{-1} after 500 cycles with a capacity retention of 76.6%. However, the most significant enhancement in both cycling performance and rate capability was observed in the Ti- and S-substituted LMTOS cathode, where the 10th discharge capacity was 114 mA h g^{-1} at 5C and the charge/discharge capacity was 123/122 mA h g^{-1} after 500 cycles, with a capacity retention of 90.3%. In addition, the CV and EIS results showed that Ti and S multisubstitution can increase Li^+ diffusion and decrease the internal resistance of the cathode during cycling. Ti substitution in LMO improved the cycling performance by stabilizing the structure and reducing volume changes. Ti and S multisubstitutions synergistically enhanced electrochemical performance, resulting in remarkable improvements in cycling performance and rate capability. These results suggested that the LMTOS cathode exhibited reduced internal resistance and potential differences efficient lithium-ion diffusion, improved charge/discharge characteristics, and sustained capacity over time. Collectively, these findings indicated the increased stability of the cathode material structure, highlighting it as a promising and robust component in battery systems.

Author contributions

Conceptualization: J. P. N., O. B. N. and J. H. Y.; data curation: J. P. N., G. H. K. and H. M. J.; funding acquisition: H. M. J., T. H. N. and J. P. N.; investigation: O. B. N., J. P. N., J. S. K., K. M. G., and I. G. B.; methodology: G. H. K., J. P. N., O. B. N., J. H. Y., and T. H. N.; supervision: J. P. N.; writing – original draft: O. B. N. and J. P. N.; writing – review & editing: J. P. N., H. M. J., J. H. Y. and G. H. K.

Conflicts of interest

The authors declare that they have no known competing financial interests or personal relationships that could have appeared to influence the work reported in this paper.

Acknowledgements

This research was funded by the National Research Foundation of Korea (NRF) grant funded by the Korean Government (MSIT) (No. 2022R1A2C1008125) and the Korea Institute for Advancement of Technology (KIAT) grant funded by the Korean Government (MOTIE) (P0012748, The Competency Development Program for Industry Specialists).

References

1 H.-W. Lee, P. Muralidharan, R. Ruffo, C. M. Mari, Y. Cui and D. K. Kim, Ultrathin spinel $LiMn_2O_4$ nanowires as high power cathode materials for Li-ion batteries, *Nano Lett.*, 2010, **10**(10), 3852–3856.

2 Y. Tao, Q. Liu, Y. Guo, M. Xiang, X. Liu, W. Bai, J. Guo and S. Chou, Regulation of morphology evolution and Mn dissolution for ultra-long cycled spinel $LiMn_2O_4$ cathode materials by B-doping, *J. Power Sources*, 2022, **524**, 231073.
3 H. Y. Asl and A. Manthiram, Reining in dissolved transition-metal ions, *Science*, 2020, **369**(6500), 140–141.
4 S. Guo, S. Zhang, X. He, W. Pu, C. Jiang and C. Wan, Synthesis and characterization of Sn-doped $LiMn_2O_4$ cathode materials for rechargeable Li-ion batteries, *J. Electrochem. Soc.*, 2008, **155**(10), A760.
5 J. Jiang, W. Li, H. Deng, G. Gong and N. Li, Research on improving the electrochemical performance of $LiMn_2O_4$ via Cr-doping, *J. Nanosci. Nanotechnol.*, 2019, **19**(1), 125–129.
6 Q. Jiang, D. Liu, H. Zhang and S. Wang, Plasma-assisted sulfur doping of $LiMn_2O_4$ for high-performance lithium-ion batteries. *The*, *J. Phys. Chem. C*, 2015, **119**(52), 28776–28782.
7 J. Lu, C. Zhan, T. Wu, J. Wen, Y. Lei, A. J. Kropf, H. Wu, D. J. Miller, J. W. Elam and Y.-K. Sun, Effectively suppressing dissolution of manganese from spinel lithium manganate via a nanoscale surface-doping approach, *Nat. Commun.*, 2014, **5**(1), 5693.
8 M. Reddy, S. S. Manoharan, J. John, B. Singh, G. S. Rao and B. Chowdari, Synthesis, Characterization, and Electrochemical Cycling Behavior of the Ru-Doped Spinel, Li [Mn2− x Ru x] O4 (x= 0, 0.1, and 0.25), *J. Electrochem. Soc.*, 2009, **156**(8), A652.
9 G. Singh, A. Panwar, A. Sil and S. Ghosh, Synthesis and characterization of citric acid assisted Cr doped lithium manganese oxide spinel, *Ceramics*, 2009, **53**(4), 260–267.
10 P. Singh, A. Sil, M. Nath and S. Ray, Preparation and characterization of lithium manganese oxide cubic spinel Li1. 03Mn1. 97O4 doped with Mg and Fe, *Phys. B*, 2010, **405**(2), 649–654.
11 R. Thirunakaran, R. Ravikumar, S. Vanitha, S. Gopukumar and A. Sivashanmugam, Glutamic acid-assisted sol–gel synthesis of multi-doped spinel lithium manganate as cathode materials for lithium rechargeable batteries, *Electrochim. Acta*, 2011, **58**, 348–358.
12 H. Zhao; S. Liu; M. Tan; Z. Wang; Y. Cai and X. Liu, *Enhanced Cycling Stability of Multi-Cations Doped Spinel Lithium Manganese Oxide for Rechargeable Lithium Batteries*, Walter De Gruyter Gmbh, Berlin, Germany, 2017.
13 K. Chudzik, M. Świętosławski, M. Bakierska, M. Kubicka, M. Gajewska and M. Molenda, Surface modification and carbon coating effect on a high-performance K and S doped $LiMn_2O_4$, *Appl. Surf. Sci.*, 2020, **531**, 147138.
14 F. U. Okudur, J. D'Haen, T. Vranken, D. De Sloovere, M. Verheijen, O. Karakulina, A. Abakumov, J. Hadermann, M. K. Van Bael and A. Hardy, Ti surface doping of LiNi 0.5 Mn 1.5 O 4− δ positive electrodes for lithium ion batteries, *RSC Adv.*, 2018, **8**(13), 7287–7300.
15 Y. Zhang, H. Xie, H. Jin, X. Li, Q. Zhang, Y. Li, K. Li, F. Luo, W. Li and C. Li, Enhancing the electrochemical properties of Ti-doped $LiMn_2O_4$ spinel cathode materials using a one-step hydrothermal method, *ACS Omega*, 2021, **6**(33), 21304–21315.
16 W. Xu, H. Li, Y. Zheng, W. Lei, Z. Wang, Y. Cheng, R. Qi, H. Peng, H. Lin and F. Yue, Atomic insights into Ti doping on the stability enhancement of truncated octahedron $LiMn_2O_4$ nanoparticles, *Nanomaterials*, 2021, **11**(2), 508.
17 L. Xiong, Y. Xu, C. Zhang, Z. Zhang and J. Li, Electrochemical properties of tetravalent Ti-doped spinel LiMn 2 O 4, *J. Solid State Electrochem.*, 2011, **15**, 1263–1269.
18 R. Tyagi and S. Srinivasan, Co-doping studies to enhance the life and electro-chemo-mechanical properties of the $LiMn_2O_4$ cathode using multi-scale modeling and neuro-computing techniques, *Phys. Chem. Chem. Phys.*, 2022, **24**(31), 18645–18666.
19 X. He, J. Li, Y. Cai, Y. Wang, J. Ying, C. Jiang and C. Wan, Fluorine doping of spherical spinel $LiMn_2O_4$, *Solid State Ionics*, 2005, **176**(35–36), 2571–2576.
20 K. Okada, I. Kimura and K. Machida, High rate capability by sulfur-doping into LiFePO 4 matrix, *RSC Adv.*, 2018, **8**(11), 5848–5853.
21 M. Raja, S. Mahanty and R. N. Basu, Influence of S and Ni co-doping on structure, band gap and electrochemical properties of lithium manganese oxide synthesized by soft chemical method, *J. Power Sources*, 2009, **192**(2), 618–626.
22 M. Molenda, M. Bakierska and D. Majda, Świętosławski, M.; Dziembaj, R. Structural and electrochemical characterization of sulphur-doped lithium manganese spinel cathode materials for lithium ion batteries, *Solid State Ionics*, 2015, **272**, 127–132.
23 M. Molenda, R. Dziembaj, D. Majda and M. Dudek, Synthesis and characterisation of sulphided lithium manganese spinels $LiMn_2O_{4-y}S_y$ prepared by sol–gel method, *Solid State Ionics*, 2005, **176**(19–22), 1705–1709.
24 M. Molenda, R. Dziembaj, E. Podstawka, W. Łasocha and L. Proniewicz, Influence of sulphur substitution on structural and electrical properties of lithium-manganese spinels, *J. Phys. Chem. Solids*, 2006, **67**(5–6), 1347–1350.
25 M. Bakierska, M. Świętosławski, R. Dziembaj and M. Molenda, Nature of the electrochemical properties of sulphur substituted $LiMn_2O_4$ spinel cathode material studied by electrochemical impedance spectroscopy, *Materials*, 2016, **9**(8), 696.
26 W. Fu-Cheng, T. Jian-Kun and Z. Hai-Lang, Synthesis and electrochemical performance of Co-doped $LiMn_2O_4$ by Mg and F with one improved soild-state method, *Int. J. Electrochem. Sci.*, 2014, **9**(8), 4627–4634.
27 M. Mianwu, L. Qinhong, J. Enyuan, L. Xinyu, L. Gang and H. Huang, Effects of doping elements lanthanum and fluorine on structure and electrochemical performance of spinel $LiMn_2O_4$ cathode material, *Rare Met. Mater. Eng.*, 2009, **38**(6), 995–998.
28 W. Wen, B. Ju, X. Wang, C. Wu, H. Shu and X. Yang, Effects of magnesium and fluorine co-doping on the structural and electrochemical performance of the spinel $LiMn_2O_4$ cathode materials, *Electrochim. Acta*, 2014, **147**, 271–278.
29 O. Nyamaa, G.-H. Kang, S.-C. Huh, J.-H. Yang, T.-H. Nam and J.-P. Noh, Unraveling the Mechanism and Practical Implications of the Sol-Gel Synthesis of Spinel $LiMn_2O_4$ as

a Cathode Material for Li-Ion Batteries: Critical Effects of Cation Distribution at the Matrix Level, *Molecules*, 2023, **28**(8), 3489.

30 X. Zeng, J. Wu and Q. Hu, Effects of magnesium and chlorine co-doping on the structural and electrochemical performance of the spinel $LiMn_2O_4$ cathode materials, *Micro Nano Lett.*, 2016, **11**(12), 789–791.

31 F. A. Amaral, N. Bocchi, R. F. Brocenschi, S. R. Biaggio and R. C. Rocha-Filho, Structural and electrochemical properties of the doped spinels Li1. 05M0. 02Mn1. 98O3. 98N0. 02 (M = Ga3 +, Al3 +, or Co3 +; N= S2− or F−) for use as cathode material in lithium batteries, *J. Power Sources*, 2010, **195**(10), 3293–3299.

32 M. Bakierska, M. Świętosławski, K. Chudzik, M. Lis and M. Molenda, Enhancing the lithium ion diffusivity in $LiMn_2O_{4-y}S_y$ cathode materials through potassium doping, *Solid State Ionics*, 2018, **317**, 190–193.

33 X. F. Fan; S. X. Zhao; L. Li and C. W. Nan, Structure and electrochemical performance of modificated $LiMn_2O_4$ by S-Co codoping and nano SiO_2 surface coating, *Materials Science Forum*, Trans Tech Publications, 2012, vol. 722, pp. 1–9.

34 M. Kubicka, M. Bakierska, M. Świętosławski, K. Chudzik and M. Molenda, The temperature effect on the electrochemical performance of sulfur-doped $LiMn_2O_4$ in Li-ion cells, *Nanomaterials*, 2019, **9**(12), 1722.

35 D. Callegari, M. Coduri, M. Fracchia, P. Ghigna, L. Braglia, U. A. Tamburini and E. Quartarone, Lithium intercalation mechanisms and critical role of multi-doping in LiFe x Mn 2− x− y Ti y O 4 as high-capacity cathode material for lithium-ion batteries, *J. Mater. Chem. C*, 2022, **10**(23), 8994–9008.

36 S. Wang, J. Yang, X. Wu, Y. Li, Z. Gong, W. Wen, M. Lin, J. Yang and Y. Yang, Toward high capacity and stable manganese-spinel electrode materials: A case study of Ti-substituted system, *J. Power Sources*, 2014, **245**, 570–578.

37 Z. Yang, Y. Wang, X. Chen, H. Wu and Y. Zhang, Mg2+ and Ti4+ co–doped spinel $LiMn_2O_4$ as lithium-ion battery cathode, *ChemistrySelect*, 2019, **4**(33), 9583–9589.

38 H. Liu, J. Wang, X. Zhang, D. Zhou, X. Qi, B. Qiu, J. Fang, R. Kloepsch, G. Schumacher and Z. Liu, Morphological evolution of high-voltage spinel LiNi0. 5Mn1. 5O4 cathode materials for lithium-ion batteries: the critical effects of surface orientations and particle size, *ACS Appl. Mater. Interfaces*, 2016, **8**(7), 4661–4675.

39 T. Zhang, D. Li, Z. Tao and J. Chen, Understanding electrode materials of rechargeable lithium batteries via DFT calculations, *Prog. Nat. Sci.: Mater. Int.*, 2013, **23**(3), 256–272.

40 C. W. Cady, G. Gardner, Z. O. Maron, M. Retuerto, Y. B. Go, S. Segan, M. Greenblatt and G. C. Dismukes, Tuning the electrocatalytic water oxidation properties of AB2O4 spinel nanocrystals: A (Li, Mg, Zn) and B (Mn, Co) site variants of $LiMn_2O_4$, *ACS Catal.*, 2015, **5**(6), 3403–3410.

41 Z.-L. Chen, Y.-J. Gu, Y.-L. Huo, X.-Y. Ma and F.-Z. Wu, Enhanced electrochemical performance of manganese-based metal organic frameworks-derived spinel $LiMn_2O_4$ cathode materials by improving the Mn3+ content and oxygen vacancies, *J. Alloys Compd.*, 2022, **917**, 165485.

42 J. Liu, G. Li, H. Bai, M. Shao, C. Su, J. Guo, X. Liu and W. Bai, Enhanced cycle and rate performances of Li (Li0. 05Al0. 05Mn1. 90) O4 cathode material prepared via a solution combustion method for lithium-ion batteries, *Solid State Ionics*, 2017, **307**, 79–89.

43 Y. Wang, L. Chen, Y. Wang and Y. Xia, Cycling stability of spinel $LiMn_2O_4$ with different particle sizes in aqueous electrolyte, *Electrochim. Acta*, 2015, **173**, 178–183.

44 Y. Xiao, X. D. Zhang, Y. F. Zhu, P. F. Wang, Y. X. Yin, X. Yang, J. L. Shi, J. Liu, H. Li and X. D. Guo, Suppressing manganese dissolution via exposing stable {111} facets for high-performance lithium-ion oxide cathode, *Adv. Sci.*, 2019, **6**(13), 1801908.

45 Z.-X. Huang, X.-L. Zhang, X.-X. Zhao, Y.-L. Heng, T. Wang, H. Geng and X.-L. Wu, Hollow Na0. 62K0. 05Mn0. 7Ni0. 2Co0. 1O2 polyhedra with exposed stable {001} facets and K riveting for sodium-ion batteries, *Sci. China Mater.*, 2023, **66**(1), 79–87.

46 T.-T. Wei, X. Liu, S.-J. Yang, P.-F. Wang and T.-F. Yi, Regulating the electrochemical activity of Fe-Mn-Cu-based layer oxides as cathode materials for high-performance Na-ion battery, *J. Energy Chem.*, 2023, **80**, 603–613.

47 T.-T. Wei, P. Peng, Y.-R. Ji, Y.-R. Zhu, T.-F. Yi and Y. Xie, Rational construction and decoration of Li5Cr7Ti6O25@ C nanofibers as stable lithium storage materials, *J. Energy Chem.*, 2022, **71**, 400–410.

48 T.-F. Yi, L.-Y. Qiu, J. Mei, S.-Y. Qi, P. Cui, S. Luo, Y.-R. Zhu, Y. Xie and Y.-B. He, Porous spherical NiO@ NiMoO4@ PPy nanoarchitectures as advanced electrochemical pseudocapacitor materials, *Sci. Bull.*, 2020, **65**(7), 546–556.

49 T. f Yi, L. Shi, X. Han, F. Wang, Y. Zhu and Y. Xie, Approaching high-performance lithium storage materials by constructing hierarchical CoNiO2@ CeO2 nanosheets, *Energy Environ. Mater.*, 2021, **4**(4), 586–595.

50 Y. Zhang; H. Xie; H. Jin; Q. Zhang; Y. Li; X. Li; K. Li and C. Bao, Research Status of Spinel $LiMn_2O_4$ Cathode Materials for Lithium Ion Batteries, *IOP Conference Series: Earth and Environmental Science*, IOP Publishing, 2020, vol. 603, p. 012051.

51 N. Oyunbayar, G.-H. Kang, J.-S. Kim, K.-M. Goo, I.-G. Baek, S.-C. Huh, J.-H. Yang and T.-H. Nam, Noh, J.-p. Streamlined two-step synthesis of spinel $LiMn_2O_4$ cathode for enhanced battery applications, *Inorg. Chem. Commun.*, 2023, 111825.

52 R. Malik, D. Burch, M. Bazant and G. Ceder, Particle size dependence of the ionic diffusivity, *Nano Lett.*, 2010, **10**(10), 4123–4127.

53 M. Park, X. Zhang, M. Chung, G. B. Less and A. M. Sastry, A review of conduction phenomena in Li-ion batteries, *J. Power Sources*, 2010, **195**(24), 7904–7929.

54 A. Martinez-Juarez, C. Pecharromán, J. E. Iglesias and J. M. Rojo, Relationship between activation energy and bottleneck size for Li+ ion conduction in NASICON materials of composition LiMM '(PO4) 3; M, M' = Ge, Ti, Sn, Hf. *The*, *J. Phys. Chem. B*, 1998, **102**(2), 372–375.

55 B. Gyenes, D. Stevens, V. Chevrier and J. Dahn, Understanding anomalous behavior in coulombic efficiency measurements on Li-ion batteries, *J. Electrochem. Soc.*, 2014, **162**(3), A278.
56 A. K. Kolah, N. S. Asthana, D. T. Vu, C. T. Lira and D. J. Miller, Reaction kinetics of the catalytic esterification of citric acid with ethanol, *Ind. Eng. Chem. Res.*, 2007, **46**(10), 3180–3187.
57 Y. Ma, L. Lv, Y. Dai, Q. Zhou, J. Cheng, H. Li and W. Hu, A First-Principles Study on the Structure and Electronic Structure of Ti-Doped Spinel LiMn 2 O 4 for Li-Ion Batteries, *J. Electron. Mater.*, 2022, **51**, 77–83.
58 P. Chaturvedi, A. B. Kanagaraj, M. S. Al Nahyan, H. Al Shibli, A. A. Ashoor, H. Fadaq, S. Al Dahmani and D. S. Choi, Electrical and electrochemical properties of carbon nanotube-based free standing LTO electrodes for current collector-free Li-ion batteries, *Curr. Appl. Phys.*, 2019, **19**(11), 1150–1155.
59 O. Nyamaa, D.-H. Seo, J.-S. Lee, H.-M. Jeong, S.-C. Huh, J.-H. Yang, E. Dolgor and J.-P. Noh, High electrochemical performance silicon thin-film free-standing electrodes based on buckypaper for flexible lithium-ion batteries, *Materials*, 2021, **14**(8), 2053.
60 H. Zhao, Y. Nie, Y. Li, T. Wu, E. Zhao, J. Song and S. Komarneni, Low-cost and eco-friendly synthesis of octahedral $LiMn_2O_4$ cathode material with excellent electrochemical performance, *Ceram. Int.*, 2019, **45**(14), 17183–17191.
61 J.-S. Lee, S.-D. Yun, O. Nyamaa, J.-H. Yang, S.-C. Huh, H.-M. Jeong, T.-H. Nam, Y.-J. Ryu and J.-P. Noh, Free-Standing Li4Ti5O12/Carbon Nanotube Electrodes for Flexible Lithium-Ion Batteries, *Energies*, 2022, **15**(22), 8585.
62 Q. Ran, H. Zhao, Y. Hu, Q. Shen, W. Liu, J. Liu, X. Shu, M. Zhang, S. Liu and M. Tan, Enhanced electrochemical performance of dual-conductive layers coated Ni-rich LiNi0. 6Co0. 2Mn0. 2O2 cathode for Li-ion batteries at high cut-off voltage, *Electrochim. Acta*, 2018, **289**, 82–93.
63 H. Wen, W. Kang, X. Liu, W. Li, L. Zhang and C. Zhang, Two-phase interface hydrothermal synthesis of binder-free SnS 2/graphene flexible paper electrodes for high-performance Li-ion batteries, *RSC Adv.*, 2019, **9**(41), 23607–23613.
64 M. Chen, S. Li and C. Yang, Structure and electrochemical properties of La, F dual-doped iLa0. 01Mn1. 99O3. 99F0. 01 cathode materials, *J. Univ. Sci. Technol. Beijing, Min., Metall., Mater.*, 2008, **15**(4), 468–473.
65 Z. Hai-Lang, Z. Lei and Y. Shi-Wan, Synthesis and electrochemical study of Co-doped $LiMn_2O_4$ at room temperature and high temperature, *Int. J. Electrochem. Sci.*, 2014, **9**, 8182–8188.
66 Q. Wang, X. Zhang, Y. Xu, D. Liu, H. Dong and Y. Zhang, Synthesis and electrochemical performance of Ni and F doped LiMn 2 O 4 cathode materials, *RSC Adv.*, 2015, **5**(92), 75333–75340.
67 M.-S. Wang, J. Wang, J. Zhang and L.-Z. Fan, Improving electrochemical performance of spherical LiMn 2 O 4 cathode materials for lithium ion batteries by Al-F codoping and AlF 3 surface coating, *Ionics*, 2015, **21**, 27–35.